electronics

MDPI

Article

Analysis of Multi-Gas Molecule Interactions in Ambient Air on Solution-Processed Indium Zinc Oxide Thin-Film Transistors for High-Performance Chemical Sensors

Dongwook Kim [1], Hyunji Shin [2], Hyeonju Lee [1], Youngjun Yun [1], Jin-Hyuk Bae [3,4] and Jaehoon Park [1,*]

[1] School of Semiconductor and Display Technology, Hallym University, Chun-Choen 24252, Republic of Korea; d.kim@hallym.ac.kr (D.K.); hjlee@hallym.ac.kr (H.L.); youngjun.yun@hallym.ac.kr (Y.Y.)
[2] School of Electrical and Computer Engineering, University of Seoul, Seoul 02504, Republic of Korea; hshin09@uos.ac.kr
[3] School of Electronics Engineering, Kyungpook National University, Daegu 41566, Republic of Korea; jhbae@ee.knu.ac.kr
[4] School of Electronic and Electrical Engineering, Kyungpook National University, Daegu 41566, Republic of Korea
* Correspondence: jaypark@hallym.ac.kr; Tel.: +82-33-248-2357

Abstract

Unencapsulated solution-processed oxide-semiconductor transistors suffer from cross-sensitivity and baseline instability. In this study, we systematically investigate the field-effect transport kinetics and species-dependent gas interaction dynamics of solution-processed amorphous indium zinc oxide thin-film transistors across pressure state transitions (760–10^{-3} Torr) and single-gas purging environments (N_2, O_2, Ar, CO_2, and humid air > 90% relative humidity). Our experimental findings indicate that atmospheric pressure variations dictate bulk channel conduction via free-carrier density shifts, whereas relative humidity drives parasitic gate (I_G)/surface leakage currents ($I_{surface}$) through moisture-mediated interfacial trap creation. Purging tests reveal a nonpolar sensing window where N_2 promotes bulk carrier accumulation, while Ar drives carrier depletion without degrading gate dielectric insulation. Electrophilic O_2 suppresses channel current while increasing I_G, whereas CO_2 exhibits total electrical invariance. Real-time pulse-switching measurements confirm high detection fidelity (maximum signal-to-noise ratio > 30 dB for N_2 and Ar) with excellent recovery. Correlating these dynamic responses with an exponential sub-bandgap density-of-states model establishes key principles for developing unencapsulated oxide chemical sensors that can discriminate complex gas–species mixtures in real-world ambient environments.

Keywords: indium zinc oxide; thin-film transistor; solution-processed semiconductor; chemical gas sensor; gas–molecule interaction; density of states

Academic Editor: Yi Gu

Received: 21 August 2026
Revised: 16 September 2026
Accepted: 16 September 2026
Published: 19 September 2026

1. Introduction

Amorphous oxide semiconductors such as indium gallium zinc oxide and indium zinc oxide (IZO) have established a dominant paradigm in next-generation electronics because of their high field-effect mobility, optical transparency, low subthreshold swing, and superior spatial uniformity over large-area substrates [1–3]. The spherical s-orbital overlap of heavy metal cations (In^{3+} 5s) enables robust conduction pathways that remain relatively insensitive to local bond-angle distortions inherent in amorphous glass-like networks [4,5]. Beyond traditional vacuum-sputtered thin-film transistor (TFT) backplanes

for high-resolution displays, solution-processed (SP) oxide semiconductors fabricated via low-cost sol–gel spin-coating and ambient thermal annealing have attracted substantial research interest as scalable, printable, and flexible electronic platforms [6,7]. Solution processing eliminates the need for capital-intensive high-vacuum deposition facilities; however, sol–gel-derived amorphous metal-oxide films intrinsically retain residual hydroxyl (–OH) groups, unpassivated metal dangling bonds, and elevated densities of sub-bandgap oxygen vacancy (V_O) defects, which render their electronic transport kinetics exceptionally sensitive to the surrounding chemical atmosphere [8,9].

This enhanced environmental sensitivity makes SP-oxide TFTs promising transducers for real-time chemical and environmental gas sensors [10–14]. Compared with conventional two-terminal chemiresistive sensors that rely on resistance modulation, three-terminal TFT chemical sensors offer multiparameter signal extraction, including threshold voltage (V_{TH}), turn-on voltage (V_{ON}), field-effect mobility, subthreshold swing, and gate leakage current (I_G), enabling richer diagnostic signatures and amplified transduction efficiency [15–17]. In typical atmospheric environments, ambient gas molecules (e.g., O_2, H_2O, N_2, Ar, and CO_2) dynamically interact with ultrathin (20–30 nm) active oxide channels through physisorption, chemisorption, and oxygen vacancy exchange kinetics [18–20]. Electrophilic oxygen molecules act as electron traps ($O + e^- \rightarrow O^-$), constructing a surface depletion layer that shifts V_{ON} positively and depresses channel current [21,22]. Conversely, ambient moisture (H_2O) exerts complex dual mechanisms: dipolar water molecules induce donor-like passivating shifts along with parasitic surface ionic/electronic conduction via Grotthuss-type proton-hopping networks [23,24].

Despite significant progress in oxide-semiconductor gas sensors, disentangling the overlapping electrical contributions of individual gas species in unencapsulated real-world operating environments remains a critical challenge [25]. A major limitation of conventional gas-sensing systems arises from testing devices exclusively against target analyte pulses diluted in humid ambient air, where strong water dipole interactions and oxygen-depletion bending frequently mask the intrinsic transport responses of nonpolar or weakly interacting ambient constituents [26]. Although the effects of electrophilic O_2 and polar H_2O are widely documented, the fundamental effects of nonpolar atmospheric species, most notably N_2 (~78% of ambient air) and Ar, on the bulk carrier density and interfacial defect kinetics of ultrathin IZO TFTs remain poorly understood [27]. Moreover, establishing a precise physical framework that decouples the bulk-channel free-carrier modulation from parasitic interface/dielectric leakage current pathways is essential for eliminating cross-sensitivity and background calibration drifts in practical sensor applications [28].

In this study, we present a comprehensive investigation of multigas molecule interactions on SP amorphous IZO (SP-IZO) TFT chemical sensors operated across systematically controlled atmospheric pressure state transitions (760 Torr $\rightarrow 10^{-3}$ Torr) and single-gas purging environments (N_2, O_2, Ar, CO_2, and humid air >90% RH). We isolated the distinct operational modulation signatures of each gas species using a custom-designed environmental vacuum probe station integrated with a precise mass flow controller (MFC). We demonstrate that ambient pressure variations dictate bulk channel conduction via drain current modulation (bulk free carrier shifts), whereas relative humidity governs parasitic/leakage current modulation (I_G and $I_{surface}$) through interfacial recombination-generation (R-G) pathways [29,30]. Crucially, we identify a distinct nonpolar sensing window in which N_2 and Ar modulate free carriers with opposite polarities (N_2-driven carrier enhancement vs. Ar-driven carrier suppression) with high signal fidelity (SNR > 30 dB), whereas CO_2 exhibits complete electrical invariance. Finally, this study establishes a unified electronic transport model and practical design criteria for highly selective, stable oxide-semiconductor chemical sensors operating in complex ambient environments by

correlating the dynamic pulse-switching kinetics (8000 s) with an exponential sub-bandgap density of states (DOS) model and Shockley–Read–Hall (SRH) recombination physics.

2. Experimental Details

2.1. Preparation of Sol-Gel IZO Precursor Solutions

Amorphous IZO precursor solutions were synthesized via a sol–gel route by dissolving indium nitrate hydrate (0.301 g, 0.1 M) ($In(NO_3)_3 \cdot xH_2O$, Sigma-Aldrich, St. Louis, MO, USA) and zinc nitrate hydrate (0.301 g, 0.1 M) ($Zn(NO_3)_2 \cdot xH_2O$, Sigma-Aldrich, St. Louis, MO, USA) in 10 mL of 2-methoxyethanol (2-ME, Sigma-Aldrich, St. Louis, MO, USA) as the primary solvent (Figure 1a, Step 1). The concentrations of the zinc and indium precursors were maintained at fixed molarities of 0.25 and 0.1 M, respectively. The solution was magnetically stirred at 60 °C for more than 6 h in a sealed glass vessel prior to thin-film deposition to ensure complete precursor dissolution, hydrolysis, and homogeneous mixing into a stable sol state.

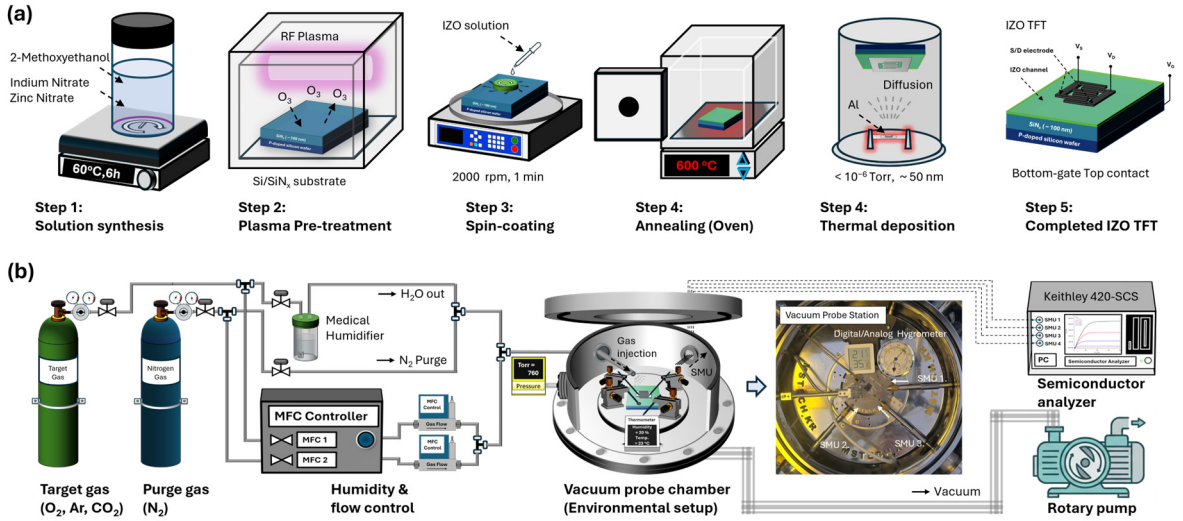

Figure 1. Sol–gel synthesis, fabrication workflow, and environmental characterization apparatus for bottom-gated SP-IZO TFTs. (**a**) Schematic of the five-step solution-processing sequence. (**b**) Custom-designed environmental vacuum measurement chamber equipped with gas manifold, microprobe station, and external semiconductor parameter analyzer feedthrough.

2.2. Fabrication of Bottom-Gate Top-Contact IZO TFTs

The fabrication sequence of the SP-IZO TFTs is depicted in Figure 1a. Heavily doped p-type silicon (p^+-Si) substrates coated with a 100-nm-thick sputtered silicon nitride (SiN_x) layer served as the common gate electrode and dielectric. Substrates were sequentially cleaned by sonication in deionized water, acetone, and isopropanol for 15 min each, followed by ultraviolet-ozone (UV/O_3) treatment for 20 min to remove organic contaminants and generate surface hydroxyl (−OH) groups, thereby enhancing surface energy and precursor wettability (Figure 1a, Step 2). The homogeneous IZO precursor solution was spin-coated onto the pretreated p^+-Si/SiN_x substrate at 2000 rpm for 60 s (Figure 1a, Step 3). The spin-coated gel films were prebaked at 120 °C for 10 min to evaporate the residual solvent, followed by high-temperature thermal annealing at 600 °C for 1 h in ambient air. This thermal treatment drives olation/oxidation condensation reactions, eliminating organic species and forming a dense metal–oxygen–metal amorphous semiconductor framework (Figure 1a, Step 4). Finally, metallic source and drain electrodes were thermally evaporated through a fine metal shadow mask under a high-vacuum base pressure of ~10^{-6} Torr to

complete the bottom-gate top-contact TFT architecture. Optical images of the fabricated SP-IZO TFT and probe station setup are presented in Figure S1, Supplementary Materials.

2.3. Environmental Gas Purging and Electrical Characterization Setup

As illustrated in Figure 1b, real-time electrical characterizations were conducted using a custom-built environmental characterization apparatus with a vacuum probe station (M6VC, MStech, Gyeonggi-do, Republic of Korea), pressure-dependent transfer/output sweeps, and gas-purging dynamic measurements. The device was mounted on a stage inside a sealed stainless-steel vacuum chamber equipped with microprobe manipulators. The chamber pressure was precisely regulated from high vacuum (10^{-3} Torr or < 10 mTorr) up to ambient atmospheric pressure (760 Torr) using a rotary vacuum pump and exhaust throttle valves. Controlled gas species (N_2, O_2, Ar, and CO_2) and humidified air (>90% RH) were introduced directly over the TFT channel via a gas spray delivery manifold connected to calibrated digital MFCs (MFC1 and MFC2, operating at 10–100 sccm). Additionally, the chamber and substrate temperatures were monitored during testing using stage-integrated sensors and analog/digital thermometers, confirming that the temperature remained stable at room temperature (26.2 $\pm$ 0.4 °C) across extended measurement runs (Figures S2 and S3, Supplementary Materials). Electrical transfer (I_D–V_G, $\sqrt{I_D}$–V_G), output (I_D–V_D), and transient pulse-response measurements were conducted using a semiconductor parameter analyzer (Keithley 4200A-SCS, Tektronix, Beaverton, OR, USA) interfaced through vacuum electrical feedthrough cables. This controlled probe station setup prevented unintended ambient degradation while enabling the precise isolation of individual gas–molecule interactions in the IZO channel. A summary of the extracted electrical parameters pristine devices is provided in Supplementary Materials Table S1.

2.4. Gas Flow Control, Chamber Pressure Dynamics, and Switching Process

To evaluate the pressure-dependent electrical characteristics, high-purity (>99.9%) gas species (N_2, O_2, Ar, and CO_2) with certified moisture traps (<1 ppm H_2O) were purged using an MFC controller at a 100 sccm flow rate starting from the initial high-vacuum state (~1 mTorr). The electrical characteristics were recorded as gas was introduced in controlled incremental steps up to 100 sccm to control the pressure on a logarithmic scale. Gas purging was continued until the chamber pressure reached ambient atmospheric pressure (760 Torr), with the total pressure-transition measurement taking over 30 min per gas species.

For the dynamic pulse-switching tests evaluating real-time gas sensor operation, measurements were initiated from the 1mTorr base vacuum condition and purged for 10 min at a constant flow rate of 100 sccm. The initial chamber pressure immediately following the opening of the check valve was approximately 100 mTorr, reaching peak sustained pressures of ~120 Torr, ~72 Torr, ~7.6 Torr, and ~9.8 Torr for N_2, O_2, Ar, and CO_2, respectively, over the 10-min gas exposure period.

3. Result and Discussion

3.1. Ambient Pressure Transitions and Moisture-Mediated Electrical Behavior

As shown in Figure 2, electrical transfer (I_D–V_G) and output (I_D–V_D) characteristics are measured across controlled pressure state transitions ranging from ambient air pressure (760 Torr) down to high vacuum (10^{-3} Torr), followed by subsequent atmospheric recovery to systematically interpret the effects of ambient atmospheric species and relative humidity (RH) on the field-effect transport kinetics of SP-IZO TFTs. The electrical parameters under air and humid states are summarized in Table 1. The observed Vth and V_{on} shift represent a combined effect of semiconductor charges (Q_{semi}), interfacial/fixed/mobile trap charge (Q_t), and effective surface potential modulation. Rather than direct chemical reaction with

N_2, single-gas purging modulates Vth through physisorption and desorption of ambient vacancy traps, establishing empirical baseline signatures for subsequent electrical analysis.

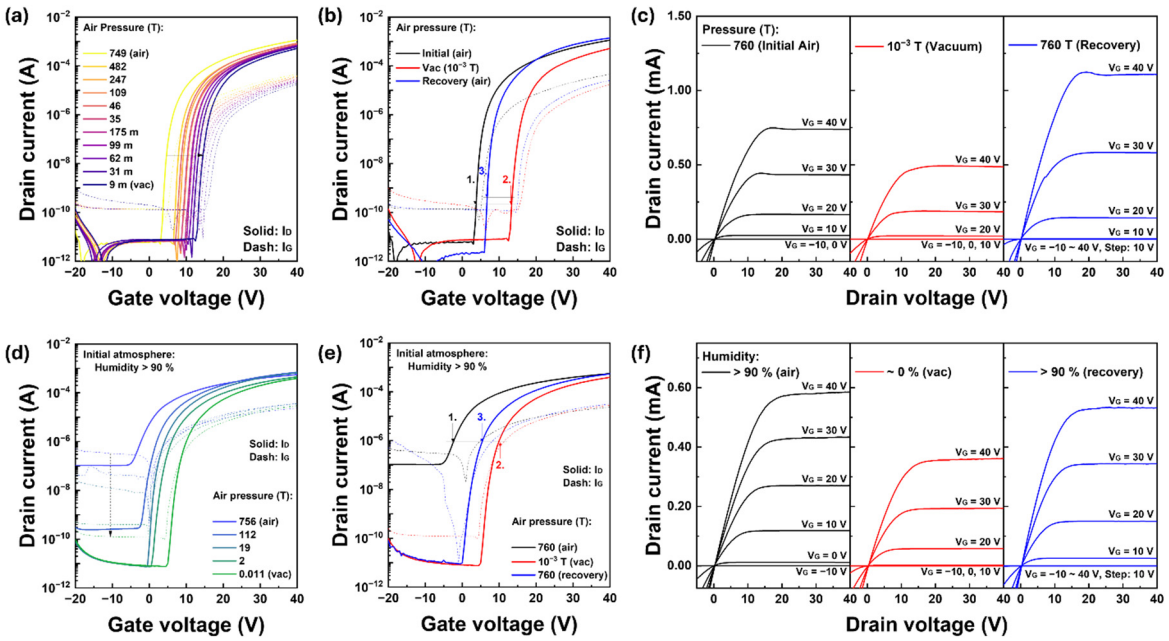

Figure 2. Ambient pressure-dependent electrical characteristics of SP-IZO TFTs. Electrical behavior under dry ambient air atmosphere: (**a**) pressure-dependent transfer curve shifts; (**b**) transfer curve modulation across sequential initial ambient (760 Torr), high vacuum (10^{-3} Torr), and post-vacuum recovery states; and (**c**) corresponding output current transitions under the before-vacuum, vacuum, and recovery conditions. Comparative response under a high-humidity atmosphere (>90% RH) for the corresponding (**d**) pressure-dependent transfer curves, (**e**) state-dependent transfer modulation, and (**f**) output current transitions. All transfer curves were measured at a drain voltage of 20 V (V_D = 20 V).

Table 1. Extracted electrical parameters for SP-IZO TFTs under low and high humidity pressure state transitions.

Operational Condition	Environmental State	V_{ON} Shift Direction	Output Current	Off-State/Leakage Current (I_{OFF}, I_G)	Dominant Mechanism/Interpretation
Low-humidity air condition (<25% RH)	(1) Initial ambient (760 Torr)	Baseline	Baseline	Low baseline	Ambient N_2/O_2 surface equilibrium
	(2) High vacuum (10^{-3} Torr)	Positive shift	Decreased	Low/Stable	Vacuum desorption Bulk-free carrier modulation
	(3) Post-vacuum recovery	Reversible shift	Increased (>Initial)	Low/Stable	Extermination of surface contaminants Fill out free carriers
High-humidity condition (>90% RH)	(1) Initial ambient (760 Torr)	Negative baseline	Elevated	Significantly increased (↑↑)	Moisture-mediated surface/dielectric traps
	(2) High vacuum (10^{-3} Torr)	Positive shift	Decreased	Decreased (↓)	Removal of water molecules Leakage reduction
	(3) Post-vacuum recovery	Delayed bulk shift	Instant recovery	Instant recovery (↑)	Immediate reaction of moisture on I_G and I_D

Note: ↑ indicates an increase/enhancement, and ↓ indicates a decrease/suppression.

Figure 2a–c depicts the pressure-dependent electrical behavior of the SP-IZO TFT operated in a low-humidity ambient air atmosphere (<25% RH). The V_{TH} and V_{ON} in the

transfer curves shift in the positive gate bias direction as the chamber pressure decreases from 760 to 10^{-3} Torr (Figure 2a). This is accompanied by a noticeable decrease in the on-state drain current (I_{ON}). The pressure-dependent characterization under low humidity ambient air effectively represents a natural multicomponent gas mixture composed of ~78% N_2, ~21% O_2, and ~1% Ar/trace gases. Electrical response in multicomponent gas mixtures reflect a convolution of the individual species-dependent mechanisms, establishing single-gas baseline signatures as a prerequisite for future mixture deconvolution. We presume that nitrogen interactions play a dominant role during ambient gas exposure because N_2 is a primary constituent of ambient air (~78%). Furthermore, the entire film reacts with high sensitivity upon exposure to varying environmental conditions because the SP-IZO active channel has an ultrathin thickness of 20–30 nm.

Sequential state-dependent transfer modulation and hysteresis kinetics are detailed in Figure 2b across three consecutive operational regimes: (1) initial ambient air (760 Torr), (2) high vacuum (10^{-3} Torr), and (3) post-vacuum recovery in ambient air. As indicated in Figure 2b, the transfer curve recovers to its initial baseline state after the vacuum measurement phase. The I_{ON} and output current (I_D) shown in Figure 2c surpass their initial values after completing the vacuum cycle. We speculate that this permanent enhancement in current magnitude originates from vacuum-driven desorption and elimination of volatile surface contaminants adsorbed prior to degassing. We presume that the increased drain current is predominantly governed by an elevated concentration of free carriers generated within the bulk IZO semiconductor matrix rather than by dielectric interactions or leakage pathways because the I_G of the TFT remains low and stable in vacuum and after the recovery process. Upon degassing to 10^{-3} Torr, the desorption of these surface-trapped contamination species releases captured electrons back into the IZO channel, elevating the baseline free-electron concentration.

A comparative set of measurements was conducted under an intentionally created high-humidity atmosphere (>90% RH) to evaluate the effect of ambient humidity, as shown in Figure 2d–f. In the presence of high ambient moisture (Figure 2d), the off-state current (I_{OFF}) and I_G increased significantly, and the corresponding drain current decreased slowly across the off-state region. Mathematically, the total measured drain current I_D in the subthreshold and off-state regimes can be expressed as the superposition of the bulk channel conduction and parasitic leakage components as

$$I_D = I_{ch} + I_G + I_{surface}, \quad (1)$$

where I_{ch}, I_G, and $I_{surface}$ represent the field-effect channel current, gate dielectric leakage current, and parasitic surface conduction, respectively. We speculate that moisture-mediated trap states and condensed surface water layers significantly increase both I_G and $I_{surface}$. Decreasing the chamber air pressure (i.e., removing ambient humidity) decreased I_{OFF}, which in turn decreased the corresponding I_D, manifesting as a distinct positive transfer curve shift (Figure 2d,e). Although off-state current is typically governed by I_G, dynamic humidity-vacuum-humidity cycles revealed that off-state I_D does not instantly track IG upon moisture exposure. This dynamic disconnect indicates an additional surface conduction path $I_{surface}$, which can account for the increase of overall output current.

During the subsequent atmospheric recovery phase, the overall channel current did not instantly recover to its initial baseline state; however, the gate leakage current and output current of the TFT reacted instantly upon pressure restoration. Based on these dynamic trends, we conclude that water molecules exert a strong and immediate effect on the parasitic leakage current pathways of the device. We interpret that the atmospheric impacts on SP-IZO TFT operation are decoupled into pressure-driven drain current modulation

(free carrier density) and humidity-driven leakage current modulation, providing key insights for stable sensor design.

3.2. Species-Dependent Gas Purging Dynamics and Electrical Modulation

Real-time electrical transfer (I_D–V_G and $\sqrt{I_D}$–V_G) and output (I_D–V_D) sweeps were evaluated under controlled purging with pure N_2, O_2, Ar, and CO_2 to investigate the individual contributions of specific gaseous species present in atmospheric air; the results are shown in Figure 3. The maximum achievable purging pressure varied across gas types (8–749, 4–224, 10–26, and 8–47 Torr for N_2, O_2, Ar, and CO_2, respectively). We presume that these varying upper pressure limits are attributable to differences in relative gas densities during high-flow purging into the vacuum chamber. Note that these peak equilibrium values are treated as the effective 1 atm equivalent state for each respective gas environment, which can be normalized across species using the pressure scale factor.

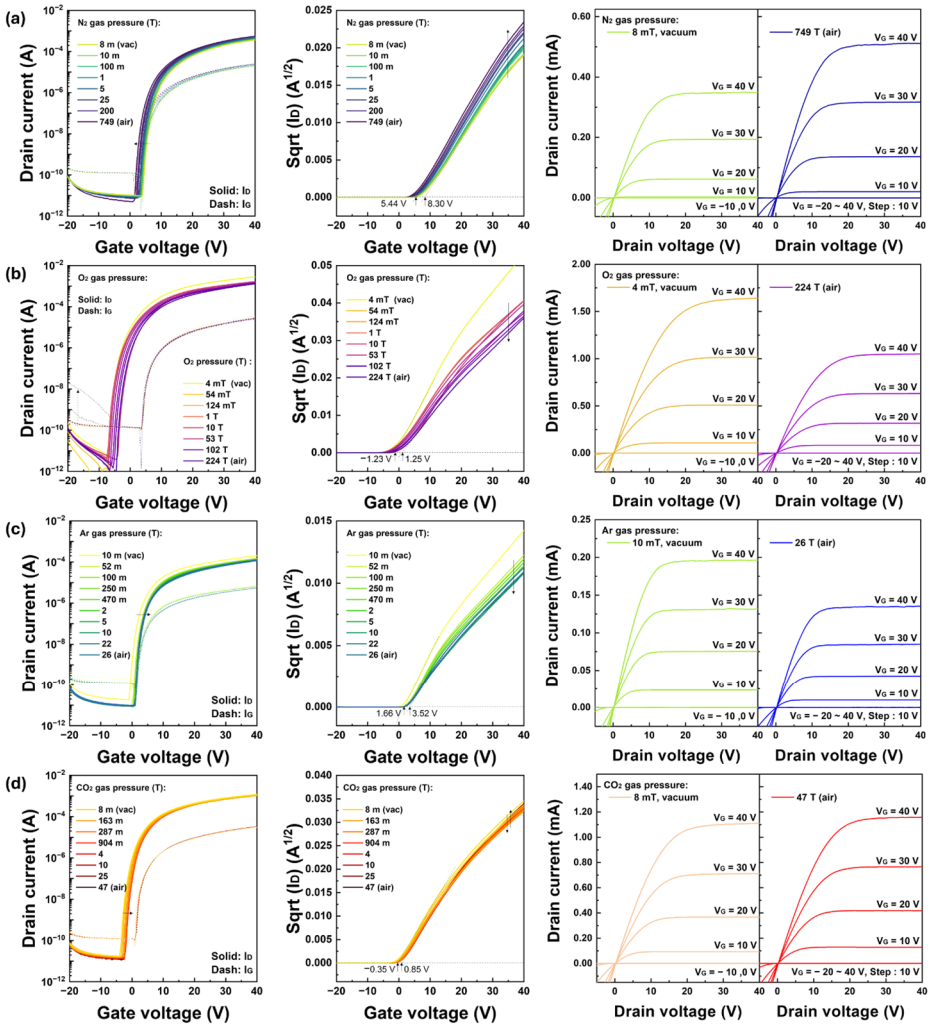

Figure 3. Electrical gate-bias drain current shifts and output modulation under controlled gas purging atmospheres. Pressure-dependent transfer (I_D–V_G and $\sqrt{I_D}$–V_G) and output current transitions measured from initial high-vacuum base conditions (<10 mTorr) up to ambient atmospheric pressure under controlled purging with (**a**) N_2, (**b**) O_2, (**c**) Ar, and (**d**) CO_2, demonstrating species-dependent dynamics. The drain voltages of transfer curves were 20 V (V_D = 20 V).

As indicated in Figure 3a, introducing N_2 gas into the evacuation chamber slightly increased the drain current and caused a minor negative shift in the transfer characteristics as the pressure increased from 8 to 749 Torr. Although V_{ON} and V_{TH} did not shift

significantly, the overall drain current magnitude in both transfer and output families increased noticeably with elevated N_2 pressure. Consistent with the experimental results of air purging, N_2 gas effectively modulated bulk carrier transport within the SP-IZO semiconductor channel.

In contrast, purging with O_2 gas (Figure 3b) induced a continuous decrease in the drain current in both transfer and output curves as the O_2 pressure increased from 4 to 224 Torr. Accompanying this current reduction, I_G increased significantly, while the baseline I_{OFF} remained relatively unchanged. Based on these observations, electrophilic O_2 gas molecules suppress carrier transport across the IZO channel.

Interestingly, Ar purging (Figure 3c) produces a carrier suppression effect similar to that of O_2, manifesting as a decrease in I_D and a positive V_{TH} shift (from 1.66 to 3.52 V). Unlike under O_2 purging, the I_G under Ar remained invariant regardless of gas pressure. We interpret this as an opposing polarity effect relative to that of N_2, where exposure to Ar gas reduced the overall effective free-carrier concentration in the bulk IZO semiconductor.

For CO_2 gas purging (Figure 3d), the electrical characteristics of the SP-IZO TFT remained remarkably stable and invariant as the pressure increased from high vacuum up to 47 Torr. Electrically, CO_2 gas did not exert any observable effect during IZO TFT operation. Unlike electrophilic O_2, CO_2 is a linear, nonpolar molecule with high thermodynamic chemical stability. We speculate that CO_2 molecules do not undergo physisorption or chemisorption charge-exchange reactions with the surface metal cations (In^{3+}, Zn^{2+}) or oxygen vacancy sites (V_O). Further, no donor- or acceptor-like states are generated upon CO_2 exposure; therefore, the free-electron concentration within the 20–30 nm ultrathin IZO channel remains unperturbed. The invariance of I_G indicates that CO_2 molecules do not penetrate or polarize the a-IZO/SiN_x dielectric interface, preventing gate stress degradation and parasitic surface leakage.

From a practical sensor design perspective, the inability of CO_2 to modulate the channel current serves as internal control, confirming that the SP-IZO TFT is selectively responsive to specific reactive or polar gas species (N_2, Ar, O_2, and H_2O) without cross-sensitivity or background interference from ambient CO_2 fluctuations. Consequently, SP-IZO chemical sensors can operate reliably in CO_2-rich environments without suffering from false-positive threshold voltage drifts or current calibration errors. From a sensor application perspective, the opposing modulation polarities observed under N_2 and Ar gases demonstrate that SP-IZO semiconductors can effectively detect these specific gaseous species. Based on these observations, the species-dependent electrical response trends and governing fundamental mechanisms for each single-gas purging environment (N_2, O_2, Ar and CO_2) are summarized in Table 2.

Table 2. Electrical response and physical mechanisms under specific gas purging environments.

Purging Gas Species	Max Pressure Achieving Air Pressure	Drain Current (I_D) Trend	V_{TH}/V_{ON} Shift Direction	Gate Leakage Current (I_G)	Proposed Effect/Sensor Application
N_2	749 Torr	Slightly increased (↑)	Negative shift	Low/Stable	Bulk carrier control Positive polarity response for gas sensing
O_2	224 Torr	Decreased (↓)	Positive shift	Significantly increased (↑↑)	Interruption of carrier transport via surface electron trapping
Ar	26 Torr	Decreased (↓)	Positive shift (1.66 → 3.52 V)	Invariant	Counter/opposite polarity effect to N_2 Bulk free carrier suppression

Table 2. *Cont.*

Purging Gas Species	Max Pressure Achieving Air Pressure	Drain Current (I_D) Trend	V_{TH}/V_{ON} Shift Direction	Gate Leakage Current (I_G)	Proposed Effect/Sensor Application
CO_2	47 Torr	Invariant	Invariant (−0.35 → 0.85 V)	Invariant	Electrically inert No charge transfer or functional interaction with IZO

Note: ↑ indicates an increase/enhancement, and ↓ indicates a decrease/suppression.

3.3. Switching Dynamics of Gas Exposure

As shown in Figure 4, time-series transient drain current (I_D, primary axis) and gate leakage current (I_G, secondary axis) responses are measured over an extended duration of 8000 s to evaluate the real-time sensing responsiveness, dynamic operational reversibility, and long-term device stability under cyclic gas exposure. The switching sequence was executed using calibrated digital MFCs operating at 100 sccm. A pressure of 100 mTorr was achieved when the gas was purged at 100 sccm and the vacuum pump was stopped. The peak sustained pressures prior to restoring the high-vacuum base conditions (~1 mTorr) were measured at 120, 72, 7.6, and 9.8 Torr for N_2, O_2, Ar, and CO_2, respectively. Although response time is conventionally defined by t90 kinetics, the temporal response profiles in this study reflect the interplay among of rapid pneumatic pressure equalization (check-valve actuation) and gradual physisorption-driven charge modulation. Thus, sensing evaluation is primarily referenced to response polarity and steady-state conductance transitions. The sudden current spikes and transient fluctuations observed upon opening and closing pneumatic check valves can be attributed to mechanical vibrations (valve bounce) occurring during pressure-state switching. Furthermore, the overall persistent decrease in the baseline I_D observed during extended temporal testing can be interpreted as carrier scattering effects and trapped carriers originating from channel-dielectric interface recombination.

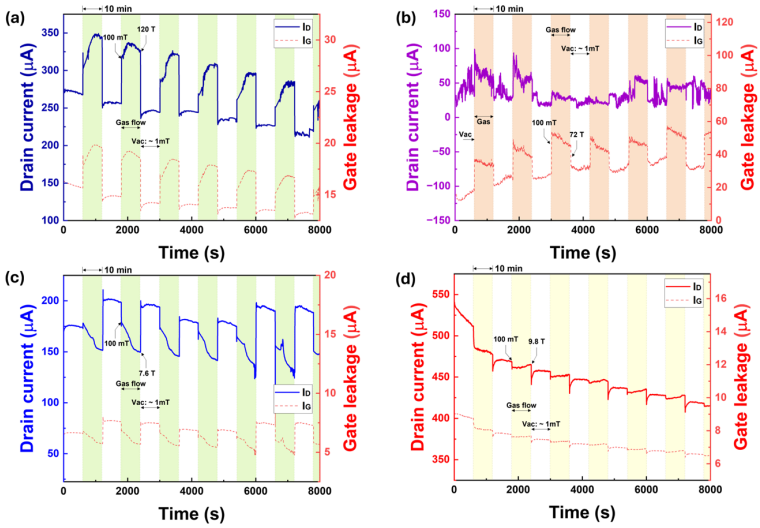

Figure 4. Transient dynamic response and pulse-modulated current characteristics under cyclic gas purging. Time-dependent transient drain current (I_D, primary axis) and gate leakage current (I_G, secondary axis) dynamics recorded over extended temporal intervals (8000 s) during periodic, pulse-modulated gas injection cycles of (**a**) N_2, (**b**) O_2, (**c**) Ar, and (**d**) CO_2. All dynamic pulse-switching measurements were conducted under a constant on-state operating bias of V_G = 20 V and V_D = 20 V. The rapid, reproducible switching between discrete high-conduction and low-conduction current states demonstrates robust operational stability, highly reversible gas-adsorption kinetics, and minimal gate-dielectric stress-induced degradation.

As indicated in Figure 4a, exposing the TFT to N_2 gas molecules substantially increases I_D from ~260 up to 350 μA. We speculate that N_2 gas effectively modulates the magnitude of I_D. Correspondingly, the I_G operates in the same direction as I_D, which we presume is driven by effective channel dimensions and bulk conduction variations under N_2 exposure. For the O_2 gas-switching operation (Figure 4b), I_D exhibited fluctuating behavior without a clear systematic trend depending on gas purging. In contrast, I_G notably follows the cyclic switching operation. Continuous current monitoring inherently exhibits reduced baseline stability compared to static electrical sweeps, such as transfer and output characteristics. TFTs experiencing dynamic charge interactions exhibit gate leakage modulation, which manifests as amplified fluctuations in the drain current. This noise-like drain current behavior may be attributed to surface electron trapping and local field redistribution at the gate-dielectric boundary.

During Ar gas purging (Figure 4c), I_D and I_G decrease simultaneously upon gas exposure. We interpret this as an opposing effect relative to that of the N_2 condition. The concurrent reduction in both I_D and I_G confirms that Ar exposure suppresses free carriers and modulates effective conduction through physical surface-interaction mechanisms. N_2 and Ar govern channel conduction through a fundamental mechanism distinct from that of electrophilic O_2 and polar moisture H_2O. Nonpolar N_2 and Ar molecules lack the strong molecular dipole moment of H_2O and the electron-withdrawing chemisorption behavior of O_2; therefore, they do not induce severe interfacial trap creation or dipolar surface conduction. Instead, we speculate that N_2 and Ar exposures effectively modulate the baseline free-carrier concentration directly within the bulk operating channel, exhibiting opposite polarity-based modulation (N_2-driven free-carrier enhancement vs. Ar-driven free-carrier suppression), offering a decoupled, highly selective sensing pathway for nonpolar gas identification.

No specific electrical transitions or systematic pulse-switching trends were observed under CO_2 gas purging (Figure 4d). Minor current fluctuations detected during CO_2 purging were affected by mechanical vibrations when the check valve was opened and closed. Electrically, CO_2 exhibits functional inertness during cyclic operations. From a chemical sensor perspective, these transient switching characteristics demonstrate that SP-IZO TFTs possess clear selectivity toward N_2 and Ar gases. The calculated signal-to-noise ratios are presented in Table 3. The Maximum signal-to-noise ratio (SNR_{Max}) was calculated using $SNR_{Max} = 20 \cdot \log_{10}(\Delta I_{signal} / \sigma_{noise})$, where ΔI_{signal} is the peak drain current modulation measured at maximum gas exposure prior to evacuation ($\Delta I_{signal} = |I_{peak} - I_{basseline}|$) and σ_{noise} is the root-mean-square of baseline current noise.

Table 3. Dynamic pulse-switching parameters, signal-to-noise ratios, and recovery kinetics under cyclic gas purge.

Sensing Gas Species	Signal Modulation (ΔI_{signal})	Baseline Noise (σ_{noise})	Maximum Decibel SNR (SNR_{Max}) (dB)	Response Characteristics
N_2	~100 μA	~2.0 μA	~34.0	Positive modulation ($\Delta I_D > 0$), high sensitivity
Ar	~55 μA	~1.4 μA	~31.9	Inverted suppression ($\Delta I_D < 0$), moderate sensitivity

N_2 and Ar exhibit opposite polarity-based switching responses (I_D enhancement vs. I_D suppression), and therefore, SP-IZO transistors are highly promising sensing elements for distinguishing specific atmospheric gas environments during dynamic switching operations.

3.4. Comprehensive Mechanisms and Electronic Transport Model

The overall electronic band structure, atomic coordination network, and charge transport pathways used to establish a unified physical model that accounts for species-dependent electrical modulation, surface adsorption kinetics, and leakage pathways observed in SP-IZO TFT sensors are illustrated in Figure 5. While direct spectroscopic surface characterization during gas purging remains challenging, the carrier modulation mechanisms can be understood through empirical field-effect transport dynamics. As demonstrated in our previous studies on energy-induced carrier excitation in SP IZO TFTs [31,32], thermal and photon energy induce carrier excitation and sub-gap state transitions, which directly translate into reproducible transfer curve shifts. Correspondingly, the observed I_D modulation under N_2 and Ar gas purging reflects on empirical carrier accumulation/depletion mechanisms driven by environment effective Fermi Energy modulation. The baseline Fermi level position $E_C - E_F \approx 1.5$ eV for 0.1 M of Indium molarity ratio and its DOS profile were quantitatively estimated via thermal and photon energy analysis.

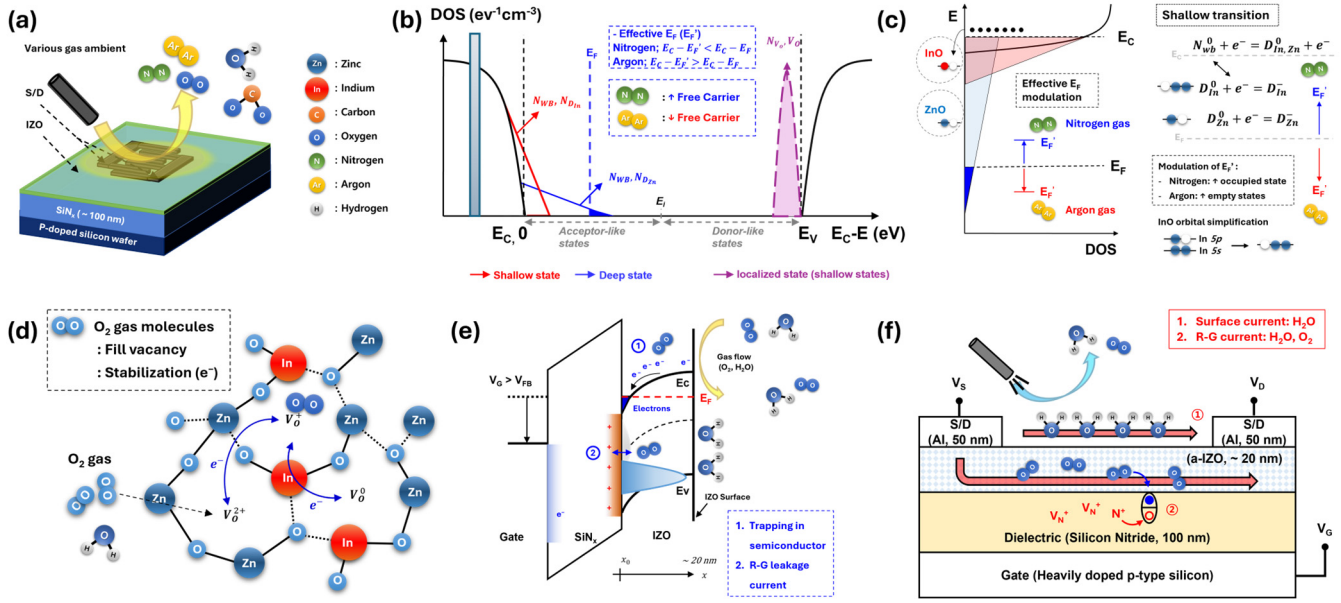

Figure 5. Comprehensive gas-sensing mechanisms and charge transport model in IZO TFTs. (**a**) Schematic of the gas shower apparatus over the TFT channel. (**b**,**c**) Effective Fermi energy (E_F') modulation and sub-bandgap charge dynamics induced by inert gas exposure. Mechanisms governing O_2 and H_2O interactions with the IZO TFT: (**d**) atomic-scale metal-oxide coordination network, (**e**) energy band bending and carrier transport interaction dynamics, and (**f**) dual-channel operational current transport pathways.

The macroscopic gas interaction setup is depicted in Figure 5a, where various ambient gas molecules (N_2, Ar, O_2, H_2O, and CO_2) are introduced over the interdigitated IZO channel via a targeted gas shower manifold. As indicated in Figure 5b, the electronic DOS within the sub-bandgap region of the amorphous IZO comprises band-tail states (N_{WB}, N_{DIn}, and N_{DZn}), states near the conduction band edge (E_C), and donor-like oxygen vacancy defect states (N_{VO}, V_O^+) near the valence band edge (E_V). The band-tail state $N_{tail}(E)$ was modeled using an exponential decay function to quantitatively describe the energy distribution of the sub-bandgap localized trap states within the SP-IZO semiconductor matrix.

$$N_{tail}(E) = N_{WB\_In} exp\left(-\frac{E_C - E}{kT_{c\_shallow}}\right) + N_{WB\_Zn} exp\left(-\frac{E_C - E}{kT_{c\_deep}}\right), \quad (2)$$

where $N_{WB\_In,}$ and N_{WB_Zn} represent the densities of the shallow- and deep-tail states at the edge of E = E_C, respectively; k represents the Boltzmann constant; and $kT_{C\_shallow}$ and kT_{C_deep} represent the characteristic decay energies that govern the energy slopes of the shallow- and deep-band tails, respectively. The total carrier density of free electrons in the equilibrium state is expressed as a sum of the mobile free electron concentration (n_c) and localized electrons (n_{loc}), n = n_c + n_{loc}, and n_c and n_{loc} was modeled by integrating the product of the conduction band density of states and band tail states with the Fermi–Dirac function.

$$n = n_c + n_{loc} = \int_{E_C}^{\infty} g_c(E) f(E) dE + \int_{E_F}^{E_C} N_{tail}(E) f(E) dE \quad (3)$$

where g_c(E) is conduction band density of states. Under zero-Kelvin Fermi–Dirac statistics (f(E) = 1 for E $\leq$ E_F and f(E) = 0 for E $\geq$ E_F), we approximate that all sub-gap states positioned energetically below the Fermi level (E $\leq$ E_F) are fully occupied by electrons, rendering them electrostatically inactive during field-effect modulation. This step-function is validated under $1/\beta << \Delta E$ ($1/\beta \equiv k_BT$, $k_BT \approx 0.0259$ eV << Eg $\approx$ 3.5 eV, at RT), where empirical temperature dependent measurements confirm thermal sub-gap excitation in SP-IZO TFT is negligible below 80 °C [31]. The integral in Equation (3) calculates the total concentration of free electrons through subgap states. We speculate that exposure to nonpolar gas species modulates the effective Fermi energy level (E_F'). Under N_2 gas purging, the effective Fermi level shifts upward toward the conduction band minimum ($E_C - E_F' < E_C - E_F$), increasing the free-electron concentration (↑free carriers) through the generation or occupation of shallow donor-like states (N_{WB}, N_{DIn}). Conversely, under Ar gas purging, the effective Fermi level deepens toward the mid-gap ($E_C - E_F' > E_C - E_F$), suppressing the free-carrier density (↓free carriers) through physical scattering and shallow-state emptying.

The corresponding band alignment and sub-bandgap charge-transition dynamics across the InO and ZnO sub-frameworks are illustrated in Figure 5c. N_2 exposure elevates E_F', enhancing the occupation of shallow and deep states through the transition pathway $N_{wb}{}^0 + e^- \rightleftharpoons D_{In,Zn}{}^0 + e^-$, $D_{In}{}^0 + e^- \rightleftharpoons D_{In}{}^-$, and $D_{Zn}{}^0 + e^- \rightleftharpoons D_{Zn}{}^-$. Ar exposure shifts E_F' downward, increasing the proportion of empty subgap states. We can adopt proper mechanisms for the free carriers by employing the effective Fermi energy E_F'.

In contrast, the IZO semiconductor exposed to O_2 gas or H_2O molecules in ambient air exhibited different mechanisms, as shown in Figure 5d–f. The amorphous IZO network consisted of interconnected In^{3+} 5*s* orbital pathways that provided high-mobility electron channels interspersed with Zn^{2+} coordination and localized oxygen vacancies ($V_O{}^+$ and $V_O{}^{2+}$). When electrophilic O_2 molecules interact within the IZO random amorphous network, they interact with the vacant oxygen sites, stabilizing the local electronic matrix ($V_O{}^0 \leftrightarrow V_O{}^+ + e^-$, $V_O{}^+ \leftrightarrow V_O{}^{2+} + e^-$) and preventing carrier generation. Under positive gate bias ($V_G > V_{FB}$), the band diagram at the a-IZO surface and SiN_x dielectric interface is presented in Figure 5e. When O_2 molecules and moisture (H_2O) are adsorbed onto the exposed IZO surface, they extract conduction band electrons, inducing trapping and forming an electron-depletion region near the excavated pathways. Thus, the accumulated positively trapped charges at the a-IZO/SiN_x interface facilitate R-G pathways, which explains the observed increase in I_G. Moreover, water molecules have a relatively strong polarity at the surface, which causes them to form a current pathway.

Figure 5f outlines the overall dual-channel operational current transport pathways under ambient atmospheric conditions. (1) Surface conduction channel (H_2O surface current): At the top surface of the ultrathin (~20 nm) IZO layer, adsorbed water molecule layers form a continuous, conductive Grotthuss-type proton hopping network between the surface of

the source and drain electrodes, generating a parasitic surface current path. (2) Bulk and interface leakage channels (R-G current: H_2O, O_2): Within the bulk semiconductor and at the a-IZO/SiN_x dielectric interface, the interface trap states ($V_N{}^+$ and N^+) modulate the trap-assisted R-G leakage current. The trap-assisted recombination rate (R_R) responsible for the parasitic interface leakage current can be described by the SRH kinetics as

$$R_R = -\sigma_n \nu_{th} N_t \Delta n \equiv -\frac{\Delta n}{\tau_R}, \quad (4)$$

where σ_n, Vth, N_t, Δn, and τ_{rec} represent the electron capture cross-section, thermal velocity of charge carriers, density of interfacial trap states, nonequilibrium excess electron concentration, and effective carrier recombination lifetime, respectively. Adsorbed moisture H_2O or O_2 molecules increase the effective interface state density, shortening τ_R and promoting additional recombination pathways that elevate gate leakage current. The SP-IZO TFT chemical sensors operate via two decoupled conduction regimes: pressure-driven bulk-free carrier modulation (governed by N_2 and Ar) and surface/interface leakage current modulation (governed by O_2 and H_2O). This comprehensive model provides clear design criteria for developing highly stable and selective oxide semiconductor gas sensors.

Systematic evaluation of electrical field-effect transport kinetics, species-dependent gas interactions, and dynamic switching stability in SP-IZO TFTs across controlled pressure state transitions (760 $\rightarrow$ 10^{-3} Torr) and specific gas purging environments (N_2, O_2, Ar, CO_2, and H_2O) reveals distinct operational regimes. Pressure state transitions demonstrate that ambient air pressure variations govern bulk channel conduction via I_D modulation (free carrier density shifts), whereas relative humidity predominantly dictates parasitic leakage current modulation (I_G and $I_{surface}$) through moisture-mediated trap state creation. Species-dependent gas purging reveals a clear polarity-based sensing window: nonpolar N_2 promotes bulk free carrier enhancement ($I_D \uparrow$), whereas nonpolar Ar drives free carrier suppression ($I_D \downarrow$, V_{TH} positive shift) without degrading gate leakage (I_G). In contrast, electrophilic O_2 interrupts channel conduction while elevating I_G, and nonpolar CO_2 exhibits complete electrical invariance. For targeted CO_2 gas-sensing applications, integrating infrared (IR)-absorbing InP-based QD layers onto an IZO channel surface can impart optical selectivity, leveraging the strong specific vibrational absorption of CO_2 molecules in the short-wave/mid-wave IR spectrum beyond 1500 nm. Dynamic pulse-modulated switching tests over extended temporal intervals (8000 s) confirmed high signal-to-noise ratios (SNR > 30 dB for N_2 and Ar) and excellent recovery reproducibility. The microscopic model and exponential DOS equations establish that SP-IZO TFT sensors operate via two decoupled conduction regimes: bulk free carrier density modulation governed by effective Fermi level ($E_F{}'$) shifts, and surface/interface trap-assisted recombination-generation leakage. Overall, this study establishes practical design criteria for developing multifunctional oxide semiconductor chemical sensors that can discriminate complex gas–species mixtures in real-world ambient air environments.

4. Conclusions

In this study, we established fundamental device physics criteria for unencapsulated oxide semiconductor chemical sensors by decoupling bulk carrier transport from surface/interface leakage pathways in SP-IZO TFTs. Our findings confirmed that atmospheric pressure fluctuations dictate bulk field-effect channel conduction via free-carrier density shifts, while relative humidity dictates parasitic leakage currents through moisture-mediated interfacial trap creation. The identification of a nonpolar sensing window, wherein N_2 and Ar modulate free carriers with opposite polarities without inducing gate-dielectric stress, offers a powerful mechanism for discriminating inert gas constituents with

high signal fidelity (SNR_{Max} > 30 dB). Furthermore, the inherent electrical invariance under CO_2 provides a stable reference baseline. Unifying these experimental transport kinetics with an exponential sub-bandgap DOS model, this study offers vital design strategies for developing stable multifunctional chemical sensors that can perform reliable operation in complex ambient atmospheric environments.

Supplementary Materials: The following supporting information can be downloaded at https://www.mdpi.com/article/10.3390/electronics15184287/s1, Table S1. Extracted electrical parameters of pristine SP IZO TFTs before test measurement of gas exposure sequence; Figure S1. Images of fabricated SP-IZO devices and chamber probe station loading. Schematic illustration of the bottom-gate top-contact amorphous IZO TFT structure under gas exposure; optical photograph of the fabricated chip array highlighting patterned C–V capacitors and TFT active areas; magnified optical top-view of an individual TFT device showing the source (V_S) and drain (V_D) electrode channels ($W/L = 25$); and internal view of the environmental vacuum probe chamber showing the device loaded onto the temperature-controlled stage with electrical SMU probe manipulators and inline gas injection lines. Figure S2. Experimental characterization setup and gas delivery apparatus. Overview of the custom-built environmental testing setup mounted on an anti-vibration table, comprising the vacuum probe chamber, high-purity gas cylinders (N_2, O_2, Ar, CO_2), mass flow controller (MFC) modules, vacuum throttling valves, pressure monitoring gauges, and the high-precision semiconductor parameter analyzer. The sealed enclosure maintains light-tight shielding and precise gas exposure control during extended temporal sweeps. Figure S3. Chamber configuration and real-time relative humidity (RH) monitoring. High-resolution photograph of the sealed vacuum probe chamber integrated with an inline digital/analog hygrometer and temperature readout. The surrounding panels display real-time digital hygrometer monitoring of the chamber interior across controlled relative humidity states ranging from minimum dry vacuum condition (<1% RH) to maximum saturated moisture purging (>95% RH).

Author Contributions: Conceptualization, D.K. and J.P.; methodology, D.K., H.S. and H.L.; software, D.K.; validation, D.K., Y.Y., J.-H.B. and J.P.; formal analysis, D.K.; investigation, D.K., H.S. and H.L.; resources, J.P.; data curation, D.K.; writing—original draft preparation, D.K.; writing—review and editing, D.K. and J.P.; visualization, D.K.; supervision, Y.Y., J.-H.B. and J.P.; project administration, J.P.; funding acquisition, J.P. All authors have read and agreed to the published version of the manuscript.

Funding: This research was supported by Hallym University Research Fund, 2026, Republic of Korea (HRF-202601-013).

Data Availability Statement: The original contributions presented in the study are included in the article and Supplementary Materials. Further inquiries and raw data supporting the reported results can be directed to the corresponding author upon reasonable request.

Conflicts of Interest: The authors declare no conflicts of interest.

Abbreviations

The following abbreviations are used in this manuscript:

DOS	Density of States
IR	Infrared
IZO	Indium Zinc Oxide
MFC	Mass Flow Controller
QD	Quantum Dot
R-G	Recombination-Generation
SNR	Signal-to-Noise Ratio
SP	Solution-Processed
SP-IZO	SP Amorphous IZO
SRH	Shockley–Read–Hall
TFT	Thin-Film Transistor

References

1. Nomura, K.; Ohta, H.; Takagi, A.; Kamiya, T.; Hirano, M.; Hosono, H. Room-temperature fabrication of transparent flexible thin-film transistors using amorphous oxide semiconductors. *Nature* **2004**, *432*, 488–492. [CrossRef] [PubMed]
2. Fortunato, E.; Barquinha, P.; Martins, R. Oxide semiconductor thin-film transistors: A review of recent advances. *Adv. Mater.* **2012**, *24*, 2945–2986. [CrossRef] [PubMed]
3. Kamiya, T.; Hosono, H. Material characteristics and device physics of amorphous indium–gallium–zinc–oxide thin-film transistors. *NPG Asia Mater.* **2010**, *2*, 15–22.
4. Park, J.S.; Maeng, W.J.; Kim, H.S.; Park, J.S. Review of recent developments in amorphous oxide semiconductor thin-film transistor devices. *Thin Solid Films* **2012**, *520*, 1679–1693. [CrossRef]
5. Kim, M.G.; Kanatzidis, M.G.; Facchetti, A.; Marks, T.J. Low-temperature fabrication of high-performance metal oxide thin-film electronics via combustion processing. *Nat. Mater.* **2011**, *10*, 382–388. [CrossRef] [PubMed]
6. Xu, W.; Li, H.; Xu, J.-B.; Wang, L. Recent Advances of Solution-Processed Metal Oxide Thin-Film Transistors. *ACS Appl. Mater. Interfaces* **2018**, *10*, 25878–25901. [CrossRef] [PubMed]
7. Arulkumar, S.; Parthiban, S.; Dharmalingam, G.; Salim, B.; Kwon, J.Y. Environmentally Stable, Solution-Processed Indium Boron Zinc Oxide Thin-Film Transistors. *J. Electron. Mater.* **2020**, *49*, 5606–5612. [CrossRef]
8. Mah, D.-G.; Lim, S.-H.; Cho, W.-J. Enhancement of Synaptic Performance through Synergistic Indium Tungsten Oxide-Based Electric-Double-Layer and Electrochemical Doping Mechanisms. *Electronics* **2024**, *13*, 2916. [CrossRef]
9. Zheng, H.; Ye, Z.; Liu, B.; Wang, M.; Zhang, L.; Liu, C. Dual-Gate Metal-Oxide-Semiconductor Transistors: Nanoscale Channel Length Scaling and Performance Optimization. *Electronics* **2025**, *14*, 1257. [CrossRef]
10. Wu, M.; Hou, S.; Yu, X.; Yu, J. Recent Progress in Chemical Gas Sensors Based on Organic Thin Film Transistors. *J. Mater. Chem. C* **2020**, *8*, 13482–13500. [CrossRef]
11. Monika, C.; Deepak; Ravi, K.C.; Umesh, K.D. Metal oxide semiconductor gas sensors: A comprehensive review of materials, mechanisms, and performance. *Mater. Sci. Semicond. Process.* **2026**, *204*, 110280. [CrossRef]
12. Dey, A. Semiconductor metal oxide gas sensors: A review. *Mater. Sci. Eng. B* **2018**, *229*, 206–217. [CrossRef]
13. Li, Y.; Liu, S.; Yang, T.; Wang, H.; Xu, Z.; Zhang, Z.; Wang, X. Humidity-Independent Chemiresistive Gas Sensors: A Review. *Materials* **2022**, *15*, 8728.
14. Saruhan, B.; Lontio Fomekong, R.; Nahirniak, S. Review: Influences of Semiconductor Metal Oxide Properties on Gas Sensing Characteristics. *Front. Sens.* **2021**, *2*, 657931. [CrossRef]
15. Mirzaei, A.; Kim, J.-Y.; Kim, H.W.; Kim, S.S. Resistive-Based Gas Sensors Using Quantum Dots: A Review. *Sensors* **2022**, *22*, 4369. [CrossRef] [PubMed]
16. Knobelspies, S.; Bierer, B.; Daus, A.; Takabayashi, A.; Salvatore, G.A.; Cantarella, G.; Ortiz Perez, A.; Wöllenstein, J.; Palzer, S.; Tröster, G. Photo-Induced Room-Temperature Gas Sensing with a-IGZO Based Thin-Film Transistors Fabricated on Flexible Plastic Foil. *Sensors* **2018**, *18*, 358. [CrossRef] [PubMed]
17. Vijjapu, M.T.; Surya, S.G.; Yuvaraja, S.; Zhang, X.; Alshareef, H.N.; Salama, K.N. Fully Integrated Indium Gallium Zinc Oxide NO_2 Gas Detector. *ACS Sens.* **2020**, *5*, 984–993. [CrossRef] [PubMed]
18. Xiao, X.; Zhang, L.; Shao, Y.; Zhou, X.; He, H.; Zhang, S. Room-Temperature-Processed Flexible Amorphous InGaZnO Thin Film Transistor. *ACS Appl. Mater. Interfaces* **2018**, *10*, 25850–25857. [CrossRef] [PubMed]
19. Barsan, N.; Weimar, U. Understanding the Fundamental Principles of Metal Oxide Based Gas Sensors; the Example of CO Sensing with SnO_2 Sensors in the Presence of Humidity. *J. Phys. Condens. Matter* **2003**, *15*, R813–R839. [CrossRef]
20. Wawrzyniak, J. Advancements in Improving Selectivity of Metal Oxide Semiconductor Gas Sensors Opening New Perspectives for Their Application in Food Industry. *Sensors* **2023**, *23*, 9548. [CrossRef] [PubMed]
21. Kang, J.H.; Cho, E.N.; Kim, C.E.; Lee, M.-J.; Lee, S.J.; Myoung, J.-M.; Yun, I. Mobility Enhancement in Amorphous InGaZnO Thin-Film Transistors by Ar Plasma Treatment. *Appl. Phys. Lett.* **2013**, *102*, 222103. [CrossRef]
22. Lee, A.P.; Reedy, B.J. Temperature Modulation in Semiconductor Gas Sensing. *Sens. Actuators B Chem.* **1999**, *60*, 35–42. [CrossRef]
23. Zhang, C.; Xu, K.; Liu, K.; Xu, J.; Zheng, Z. Metal Oxide Resistive Sensors for Carbon Dioxide Detection. *Coord. Chem. Rev.* **2022**, *472*, 214758. [CrossRef]
24. Baek, E.; Joe, S.-Y.; Kang, H.; Jeong, C.; Lee, H.; Choi, I.; Kim, S.; Park, S.; Kim, D.; Park, J.; et al. High-Detectivity Organic Photodetector with InP Quantum Dots in PTB7-Th:PC_{71}BM Ternary Bulk Heterojunction. *Polymers* **2025**, *17*, 2214. [CrossRef] [PubMed]
25. Lee, D.-H.; Kim, D.-H.; Jeong, H.-S.; Hwang, S.-H.; Lee, S.; Kim, M.-H.; Lim, J.H.; Kwon, H.-I. Comparative Study on the Separate Extraction of Interface and Bulk Trap Densities in Indium Gallium Zinc Oxide Thin-Film Transistors Using Capacitance–Voltage and Current–Voltage Characteristics. *Coatings* **2021**, *11*, 1135. [CrossRef]
26. Lin, L.; Wang, Y.; Liu, Y.; Wang, S.; Li, T.; Feng, S.; Qin, S.; Zhang, T. Heteronanostructural metal oxide-based gas microsensors. *Microsyst. Nanoeng.* **2022**, *8*, 85. [CrossRef] [PubMed]

27. Daniel, A.M.; Celso, M.A. Dependence of n-Type Metal-Oxide Gas Sensor Response on the Pressure of Oxygen and Reducing Gases. *ACS Sens.* **2024**, *9*, 1938−1944. [CrossRef] [PubMed]
28. Aroutiounian, V. Metal oxide hydrogen, oxygen, and carbon monoxide sensors for hydrogen setups and cells. *Int. J. Hydrogen Energy* **2007**, *32*, 1145–1158. [CrossRef]
29. Kim, D.; Shin, H.; Lee, H.; Yun, Y.; Bae, J.H.; Park, J. Decoupling Reversible Interface Trapping and Irreversible Bulk Transitions in Solution-Processed Indium Zinc Oxide Thin-Film Transistors. *Nanomaterials* **2026**, *16*, 877. [CrossRef] [PubMed]
30. Mori, Y.; Yoshimoto, H.; Takeda, K.; Yamada, R.I. Mechanism of random telegraph noise in junction leakage current of metal-oxide-semiconductor field-effect transistor. *J. Appl. Phys.* **2012**, *111*, 104513. [CrossRef]
31. Kim, D.; Lee, H.; Yun, Y.; Park, J.; Zhang, X.; Bae, J.-H.; Baang, S. Analyzing Acceptor-like State Distribution of Solution-Processed Indium-Zinc-Oxide Semiconductor Depending on the in Concentration. *Nanomaterials* **2023**, *13*, 2165. [CrossRef] [PubMed]
32. Kim, D.; Lee, H.; Ejderha, K.; Yun, Y.; Bae, J.-H.; Park, J. Investigation of Donor-like State Distributions in Solution-Processed IZO Thin-Film Transistor through Photocurrent Analysis. *Nanomaterials* **2023**, *13*, 2986. [CrossRef] [PubMed]